Supercavitating flow around high-speed underwater projectile near free surface induced by air entrainment

Chang Xu, Jian Huang, Yiwei Wang, Xiaocui Wu, Chenguang Huang, and Xianqian Wu

Citation: AIP Advances **8**, 035016 (2018); doi: 10.1063/1.5017182
View online: https://doi.org/10.1063/1.5017182
View Table of Contents: http://aip.scitation.org/toc/adv/8/3
Published by the American Institute of Physics

AIP ADVANCES **8**, 035016 (2018)

Supercavitating flow around high-speed underwater projectile near free surface induced by air entrainment

Chang Xu,[1,2] Jian Huang,[1,2] Yiwei Wang,[1,2,a] Xiaocui Wu,[1,2]
Chenguang Huang,[1,2] and Xianqian Wu[1,2]
[1]*Key Laboratory for Mechanics in Fluid Solid Coupling Systems, Institute of Mechanics, Chinese Academy of Sciences, Beijing 100190, China*
[2]*School of Engineering Science, University of Chinese Academy of Sciences, Beijing 100049, China*

(Received 25 November 2017; accepted 1 March 2018; published online 16 March 2018)

Cavitating flow near free surface is a complicated issue and may provide new inspiration on high-speed surface cruising. This study observes stable supercavitating flow as a new phenomenon in a launch experiment of axisymmetric projectile when the upper side of the projectile coincides with the free surface. A numerical approach is established using large eddy-simulation and volume-of-fluid methods, and good agreements are achieved between numerical and experimental results. Supercavity formation mechanism is revealed by analyzing the experiment photographs and the iso-surface of 90% water volume fraction in numerical results. The entrainment of a large amount of air into the cavity can cause the pressure inside the cavity to similarly increase with the pressure outside the cavity, which makes the actual cavitation number close to zero and is similar to supercavitation. Cases with various headforms of the projectile and cavitation numbers on the cavitating flow, as well as the drag reduction effects are further examined. Results indicate that the present strategy near the free surface could possibly be a new effective approach for high-speed cruising after vigorous design optimization in the future. https://doi.org/10.1063/1.5017182

I. INTRODUCTION

Cavitation phenomenon occurs in low-pressure regions around high-speed underwater vehicles, and extremely high pressure generated by unstable cavity and collapse can cause serious damage on vehicle surface.[1,2] The instable cavitation is one of the most important speed barrier for underwater vehicles. The typically unstable phenomena of cavitating flows include re-entry jet, cavity shedding, and internal collapse. Many researchers have studied these issues by using experimental and numerical methods.[3,4] Relevant experiments are mostly performed in water tunnels by using high-speed camera, particle image velocimetry,[5–7] and X-ray[8–10] as the main measuring instruments. The computational fluid dynamic method is mostly used for numerical simulations by solving Navier–Stokes equations which are adopted as governing equations. The cavitation model and turbulent-solving approach are key factors of numerical methods. Cavitation models are introduced to calculate mass transfer between water and vapor phases.[11–15] Two methods are mostly used in turbulence effect simulations: Reynolds-averaged Navier–Stokes (RANS) equations and turbulence models, and large-eddy simulation (LES). Physical modifications are usually necessary for RANS approaches to accurately estimate turbulent viscosity inside the cavity. Approaches, such as modified renormalization-group k-ε turbulence model,[16–20] filter-based k-ε model,[21] and partially-averaged Navier-Stokes method,[22–24] are widely used. LES is newly applied in the cavitation simulation field to capture considerable details

[a]Corresponding Author: wangyw@imech.ac.cn (Yiwei Wang).

of vortex-related cavity structures in the flow field with high accuracy. A few promising results have been published.[22,25–30]

Artificial ventilation is an important and the most widely applied control approach in the cavitating flow; this approach can be used for drag reduction to increase the cruise speed.[31] Typical categories include bubble layer drag reduction (BLDR),[32,33] air layer drag reduction (ALDR),[34–36] and artificially ventilated supercavitation.[37] An attractive prospect for friction drag reduction can be provided by replacing liquid water with gas in the flow near the vehicle surface to create a large reduction in near-wall density. Moreover, non-condensable gas can weaken or eliminate the collapse of unstable cavity to protect the vehicle surface structure. Supercavitating flow also involves complex unstable factors, such as gas leakage and shedding at the cavity closure, which has received considerable attention in recent years.[38,39]

Cavitating flow under the effect of free surface is rarely studied in the past, which may involve many complicated interfacial phenomena. The mechanism of cavity formation and collapse around a projectile in high-speed water entry is presented. Analytical and numerical methods are suggested to estimate variables that are important in characterizing the cavity dynamics.[40,41] Wang[42,43] studied in detail the free surface effect on the cloud cavitating flow around an axisymmetric projectile. Moreover, the atmospheric ventilation flow around a blunt body near the free surface was discussed. The free surface effect on the cavitating flow around hydrofoil is usually studied using potential flow theory and VOF method.[44–46] The free surface is usually considered to be a negative factor for water surface vehicles due to the large drag induced by wave elevation.[47] However, a few marine animals, such as whales and dolphins, swim fast by sliding on the free surface, which may provide new inspiration to our study.[48] Several common difficulties are far from being solved, such as large interface deformation, cavitation phase change, and interactions between the free surface and cavitation. Many complex phenomena require people to reveal. A few special and interesting new phenomena may bring significant prospects to underwater cruise.

In a launch experiment of the axisymmetric projectile, air entrainment occurred, and supercavity was generated when the free surface coincides with the upper side of the projectile. The air entrainment problem was mentioned by Faltinsen and Semenov[49] as an extreme phenomenon. The adjoined studies of experiment and numerical simulations are performed, which showed a new phenomenon and revealed the mechanism. The present work is organized as follows. Section II presents the experimental setup. Section III introduces numerical methods, and relevant flow parameters. Section IV describes cavity evolutions and analyzes the supercavity mechanism and effect. Subsection IV A compares the overall evolutions between numerical and experimental results, which focuses on the mechanism of cavity evolutions and the characteristics of fast air entrainment. Subsection IV B and IV C discussed cases with various projectile headforms and cavitation number. Subsections IV D and IV E further examine the relative vortex structures and drag reduction effects, respectively. Section V summarizes the major conclusions of the study.

II. EXPERIMENTAL SETUP

Launch system is established based on split Hopkinson pressure bar technology,[50] which can transiently accelerate the projectile with a slight disturbance on water. The present system is also adopted to investigate cloud cavitating flow near the free surface.[42] The projectile used in this study is a slender polished stainless-steel blunt head cylinder with 37 mm diameter. The free surface is tangent to the model at its upper side. The water tank test facilities are shown in Figure 1. Typical photograph with the model and cavity can be obtained, as shown in Figure 2, using a high-speed camera with 25,000 fps. The analysis of obtained images indicates that speed is approximately uniform at 19.1 m/s. The temperature is 20 °C. The cavitation number can be calculated as follows:

$$\sigma = \frac{p_\infty - p_v}{\frac{1}{2}\rho_w v^2{}_\infty} = 0.54 \tag{1}$$

where p_∞ is pressure in open air, p_v is saturated vapor pressure, ρ_w is water density, and v_∞ is projectile speed. The supercavity generated from the projectile shoulder is clearly shown. The cavity is

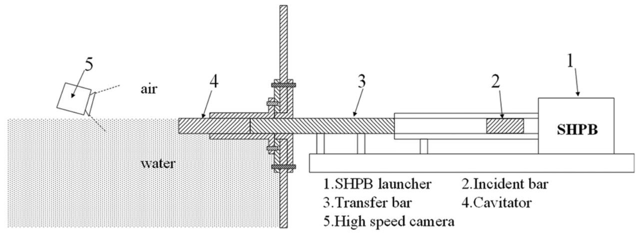

FIG. 1. Water tank test facilities.

non-asymmetrically affected by the free surface. Thus, the lengths of the upper and lower sides of the cavity are measured, as shown in Figure 2. In this figure, L_{up} is calculated based on the cavity section on the free surface level, and L_{down} is calculated based on the cavity section on the lower side level of the projectile. Length and thickness precision is approximately a pixel of the image (0.74 mm). Given that the model is small and fast, the difference between the pressure exerted by gravity at the upper and lower side of the model is nearer than flow dynamic pressure. The equation $\frac{\rho_l g d}{\frac{1}{2}\rho_l v^2{}_\infty} = 0.0018 \ll 1$ shows that variation of local cavitation number in y direction is very small. $d = 37mm$ is the projectile diameter. Cavity evolution will be mainly discussed based on experimental pictures and numerical results in the following sections. The cavity shape changes with the submerged depth at the launch, and the cavitation phenomenon can be classified by shape development into cloud cavitation,[42] natural ventilation[43] and supercavitation. Moreover, cavitating flow depends on the headforms of the projectile and cavitation number, which are discussed in Sections IV B and IV C, respectively.

III. NUMERICAL METHODS

A. Governing equations

Mixture/multiphase flow equations are adopted to simulate the motions of liquid water, vapor, and air, including the phase change. Continuity and momentum equations for the mixture are established as follows.

$$\frac{\partial \rho}{\partial t} + \frac{\partial \left(\rho u_j\right)}{\partial x_j} = 0 \tag{2}$$

$$\frac{\partial (\rho u_i)}{\partial t} + \frac{\partial \left(\rho u_i u_j\right)}{\partial x_j} = -\frac{\partial p}{\partial x_j} + \frac{\partial}{\partial x_j}\left(\mu \frac{\partial u_j}{\partial x_j}\right) \tag{3}$$

where u_i is the velocity component in the i direction, and p is pressure.

Laminar viscosity μ is defined as a volume-weighted average of the three components as

$$\mu = (1 - \alpha_v - \alpha_a)\,\mu_l + \alpha_v \mu_v + \alpha_a \mu_a \tag{4}$$

where α_v and α_a are vapor and air volume fractions, respectively.

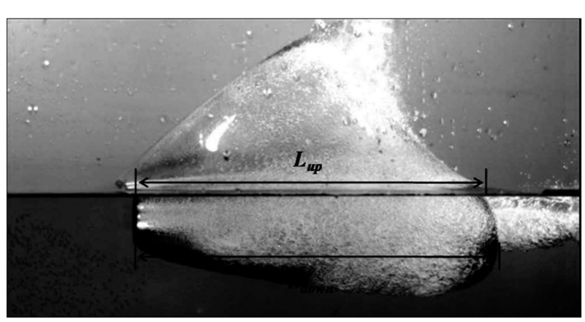

FIG. 2. Typical cavitation photograph.

Mixture density ρ is defined as

$$\rho = (1 - \alpha_v - \alpha_a)\,\rho_l + \alpha_v \rho_v + \alpha_a \rho_a \tag{5}$$

The volume fractions of vapor and air are governed by the following mass transfer equations:

$$\frac{\partial(\alpha_v \rho_v)}{\partial t} + \frac{\partial\left(\alpha_v \rho_v u_j\right)}{\partial x_j} = \dot{m}^+ - \dot{m}^- \tag{6}$$

$$\frac{\partial(\alpha_a \rho_a)}{\partial t} + \frac{\partial\left(\alpha_a \rho_a u_j\right)}{\partial x_j} = 0 \tag{7}$$

The source terms $\dot{m}^+$ and $\dot{m}^-$ in the vapor transport equation (6) represent the mass transfer rate of evaporation and condensation, respectively, which are derived from the bubble dynamics equations of generalized Rayleigh–Plesset equation by Zwart et al.[51] as follows.

$$\dot{m}^+ = F_{vap} \frac{3a_{nuc}\,(1 - \alpha_v)\,\rho_v}{R_B} \sqrt{\frac{2}{3} \frac{max\,(p_v - p, 0)}{\rho_l}} \tag{8}$$

$$\dot{m}^- = F_{cond} \frac{3\alpha_v \rho_v}{R_B} \sqrt{\frac{2}{3} \frac{max\,(p - p_v, 0)}{\rho_l}} \tag{9}$$

The generalized bubble radius R_B in Equations (8) and (9) is set at 10^{-6} m, the nucleation site volume fraction a_{nuc} is set at 5×10^{-4}, the evaporation coefficient is set at 50 m, and the condensation coefficient is set at 0.01. The selected parameter values are based on the work of Zwart et al. These parameters have been discussed and are found to work well for a variety of fluids and devices. The parameters and the recommended value of the cavitation model are extensively used.[42] A few studies have shown that the parameters within a certain range have a slight effect on the results of cloud cavitating flow.[52]

B. LES approach

The governing equations are solved by the LES approach with the Smagorinsky–Lilly subgrid scale (SGS) model. Applying a Favre-filtering operation to Equations (2) and (3) derives the following LES equations:

$$\frac{\partial \rho}{\partial t} + \frac{\partial\left(\rho \bar{u}_j\right)}{\partial x_j} = 0 \tag{10}$$

$$\frac{\partial(\rho \bar{u}_i)}{\partial t} + \frac{\partial\left(\rho \bar{u}_i \bar{u}_j\right)}{\partial x_j} = -\frac{\partial \bar{p}}{\partial x_j} + \frac{\partial}{\partial x_j}\left(\mu \frac{\partial \bar{u}_j}{\partial x_j}\right) - \frac{\partial \tau_{ij}}{\partial x_j} \tag{11}$$

where the over bars denote filtered quantities. The SGS stress τ_{ij}, which must be modeled as the extra term in Equation (11), is defined as follows.

$$\tau_{ij} = \rho(\overline{u_i u_j} - \bar{u}_i \bar{u}_j) \tag{12}$$

The Boussinesq hypothesis is employed, in which the SGS stress is computed from

$$\tau_{ij} - \frac{1}{3}\tau_{kk}\delta_{ij} = -2\mu_t \bar{S}_{ij} \tag{13}$$

where μ_t is the SGS turbulent viscosity. Isotropic part kk is not modeled but added to the filtered static pressure term. Sij is the rate-of-strain tensor for the resolved scale, which is defined by

$$\bar{S}_{ij} \equiv \frac{1}{2}\left(\frac{\partial \bar{u}_i}{\partial x_j} + \frac{\partial \bar{u}_j}{\partial x_i}\right) \tag{14}$$

The SGS turbulent viscosity μ_t is closed by the Smagorinsky–Lilly model and calculated by $\mu_t = \rho {L^2}_s \sqrt{2\bar{S}_{ij}\bar{S}_{ij}}$, where L_s is the mixing length for the subgrid scales. It is computed by $L_s = \min(\kappa d, C_s V^{1/3})$, where κ is the von Karman constant, d is the distance to the closet wall, C_s is the Smagorinsky constant set as 0.1, and V is the volume of the computational cell.

C. Simulation procedure

The present study adopted mixture/multiphase flow equations and related approaches to simulate the motions of liquid water, vapor, and air, including the cavitation effect of phase change. The details of the numerical methods can be found elsewhere.[42] The mass transfer rates of phase change are calculated using the cavitation model derived from bubble dynamics equations of the generalized Rayleigh–Plesset equation by Zwart et al.[53] The LES equations are derived by applying a Favre-filtering operation to involve the interaction between cavitation and vortex. The Smagorinsky–Lilly model is used as an SGS model based on the Boussinesq hypothesis to calculate the SGS stress. Unsteady numerical simulations are performed based on a finite-volume method with a coupled scheme by using commercial computational fluid dynamics software from ANSYS Fluent (Canonsburg, PA, USA). The computational domain is shown in Figure 3, with half of the model considered. A semi-infinite projectile model is used, and the effect of the tail on the shoulder cavity is neglected. The model is fixed with the free surface moving toward it. For the velocity inlet boundary condition, inlet velocity is set at 19.1 m/s without turbulent perturbations. Other detailed numerical schemes and parameters are listed. Second-order implicit scheme is used for time discretization, which is compatible with the cavitation model and LES method. The body force weighted option is selected for pressure interpolation. The modified high-resolution interface-capturing scheme selected is more robust than explicit geometric reconstruction scheme and compatible with cavitation mass transfer. As whole acceleration process is very short in the experiment, the unsteady cavitating flow simulations are started from a uniform flow field. The time step size is set as 10^{-5}s.

The computational domain is discretized with a block-structured grid, which is refined around the model and near the free surface, as shown in Figure 4. The first layer height is set at 1 m to

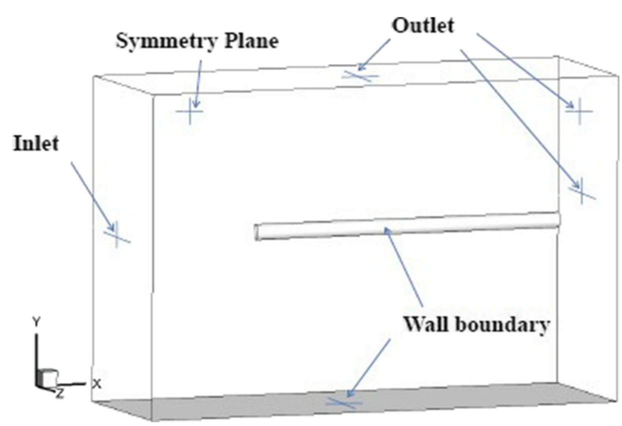

FIG. 3. Calculated domain and boundary conditions (domain size 1.2 x 0.8 x 0.4 m).

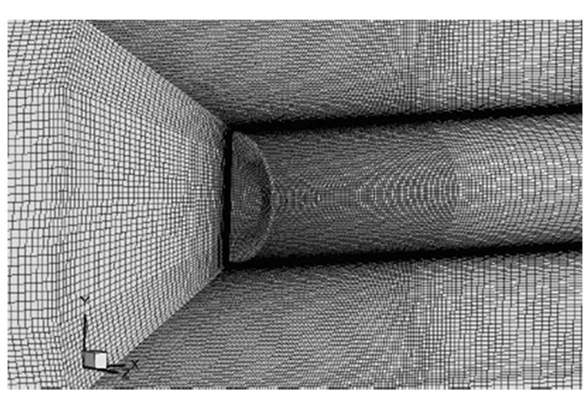

FIG. 4. Mesh near the head of the projectile.

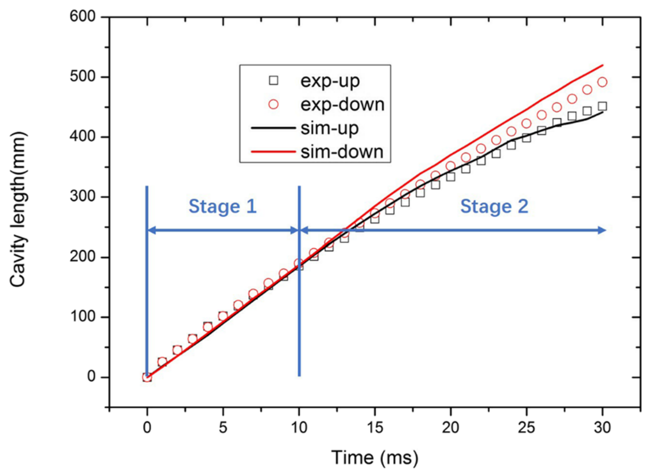

FIG. 5. The comparison of the variation of cavity lengths. Cavities on the upper and lower sides nearly have the same length in the first stage, and cavities on the lower side are notably longer than the upper side in the second stage.

ensure that Y+ is approximately equal to 1. The cell number is approximately four million with good orthogonality. Numerical method verification, including grid independence analysis, can also be found in the Ref. 42 based on cloud cavitating flow near the free surface.

D. Comparison of cavities evolution

The development of cavity shape and length is obtained from experimental and numerical results. The overall evolution and length variations of the cavity are shown in Figure 5, in which the process involves two stages. In Stage 1, the cavity rapidly grows and is approximately linear, and cavity lengths are similar on different sides of the projectile. In Stage 2, cavity growth rate decreased, and the cavity on the upper side is notably shorter than that on the lower side. The difference gradually increased with time. Length development and variation of the obtained numerical results fairly agree with the experiments, which include the relationship between upper and lower sides of the cavity.

We produce a new refined mesh that contains approximately 30 million cells using the same mesh method to verify the stability of the original mesh size for the simulation. The resultant cavity profiles are compared to that in the previous simulation and in the experimental results. Figure 6 shows the results of the comparison. The present study considers the main features of cavity evolution to a more considerable extent than in other attributes. By comparing the images shown in Figure 6 we find that the refined mesh simulation results are consistent with the original results of

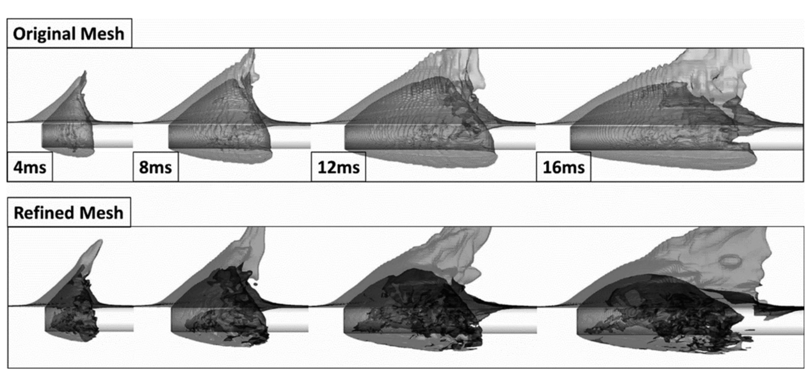

FIG. 6. Comparison of the cavity profiles between the experimental figures and the simulated results of the original mesh and refined mesh.

cavity evolution. The specific features for comparison include cavity length, cavity shape, and wave elevation.

After verifying the mesh independence of the simulation method, the simulation results of the original mesh are used for further analysis and discussion. The results show that the mesh plan is fairly stable. The simulated results of small cell sizes remain good.

IV. RESULTS AND DISCUSSION

A. Cavity development and air entrainment

The developments of cavity and free surface can be presented by experiment photographs and the iso-surface of 90% water volume fraction in numerical results. The cavity stably grows and remains transparent in the initial stage. Cavity shape under the free surface is similar to that in the common submerged case. The water layer leaps above the free surface by projectile impact. Water layer steeply rises, and the trailing edge of the water layer is nearly vertical. The water layer tip separates in the experimental photographs, and the volume fraction of the liquid water phase decreases in the same zone, as shown in Figure 7(a). The cavity continues to grow, and the intersection angle between the water layer and the horizontal plane gradually decreases. The fracture zone on top of the water layer expands downward, as shown in Figures 7(b)–7(d). The cavity does not have an apparent re-entry jet, thus remaining transparent in this process. The water volume fraction distribution around the projectile at 10 ms is shown in Figure 9(d).

The stable cavity is significantly longer than that in the submerged case, which is approximately twice the diameter of the present cavitation number. Therefore, the cavitation phase change is no longer the most important active factor of cavity development. Streamlines inside and around the projectile at typical moments are shown in Figure 8. Strong air entrainments are generated in this case. The air in the main flow turns around into the cavity through the trailing zone to the leading cavity edge. Then, the air sweeps the projectile surface in a tangential direction. Finally, air flows to the trailing edge to support the cavity part under the free surface.

The shapes of the cavity and the leaping water layer at 10 ms are similar with those at 8 ms, but the lengths are long (Figures 9(a) and 9(b)). The cavity opening can be clearly seen from the back view, as shown in Figure 9(c). The open-zone border is crimped inward. An intact cavity boundary is formed in the upstream part of the cavity by the leaping water layer and the water field under the free surface. However, the profiles breaks down in the downstream part of the cavity beyond the leaping water layer. Therefore, the external access for air entrainment is retained (Figure 9(d)).

Given that the lowest pressure is located at the leading edge of the projectile, air entrainment rapidly flows upstream after access and then turns downward. Finally, air flows downstream and leaks

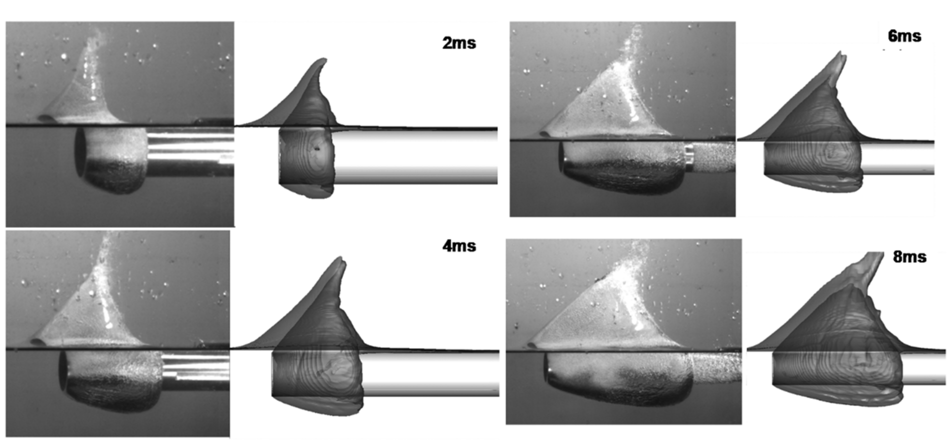

FIG. 7. Cavity development in the growth process. The left and right views are the experiment photograph and the iso-surface of 90% water volume fraction at each moment, respectively.

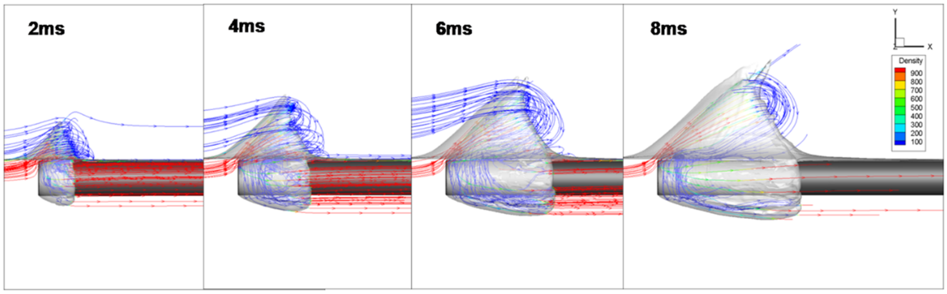

FIG. 8. Time sequences of streamlines inside and around the cavity. The color of streamlines presents the density of the mixture, in which red means that the liquid phase is dominant, whereas blue means the gas phase (vapor or air) is dominant.

outside the cavity boundary, as shown in Figure 10. Pressure levels inside and outside are similar, which makes the actual cavitation number close to zero and is similar to supercavitation (as shown in Figure 11).

The cavity continues to grow after 10 ms in the cavity evolution period we considered. The cavity on the upper side becomes notably shorter than the lower side, and the intersection angle between the water layer and the horizontal plane decreases. The broken water layer falls and evolves to a fan-shaped zone, as shown in Figure 12. Given that the drag of broken water layer is high, its velocity decreases and then falls under the gravity effect until it impacts on the upper projectile surface.

The access area becomes small due to the falling water layer. Most of the outside streamlines of air entrainments are on the sides of the cavity, as shown in Figure 13(a). The air entrainment access is partially closed when the broken water layer comes in contact with the upper projectile surface, as shown in Figure 13(b).

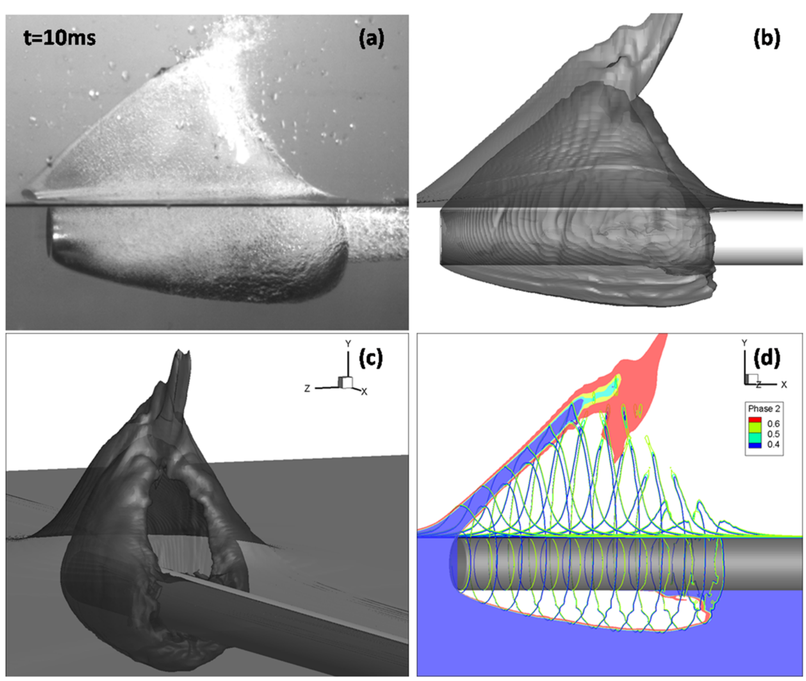

FIG. 9. Cavity patterns at 10 ms. (a) The cavity shape in the experiment photograph. (b) The cavity shape in the numerical results from the side view. (c) The cavity shape in the numerical results from the back view. (d) Flood contour of the volume fraction of the air phase with a cut-off value of 0.9, while the line contour presents the air volume fraction in the axial slices, which can show the profiles of the water layer and the cavity.

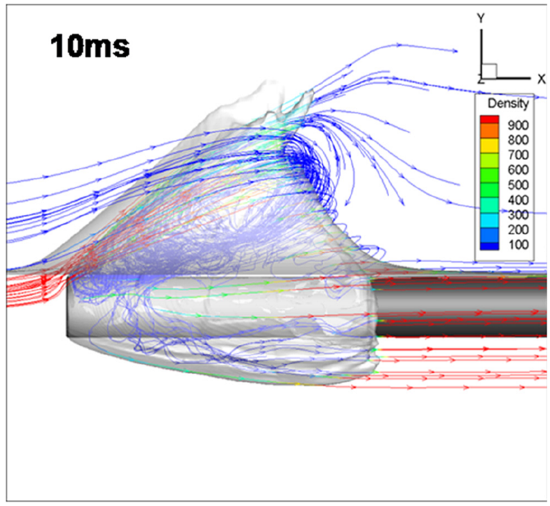

FIG. 10. Streamlines inside and around the cavity at 10 ms. The color of streamlines presents the density of the mixture, in which red means the liquid phase is dominant, while blue means the gas phase (vapor or air) is dominant.

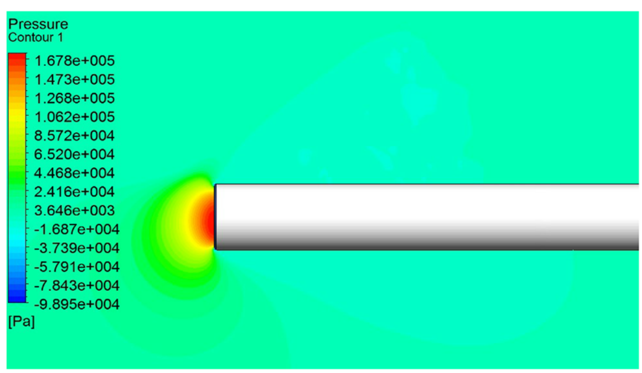

FIG. 11. Pressure distribution around the projectile.

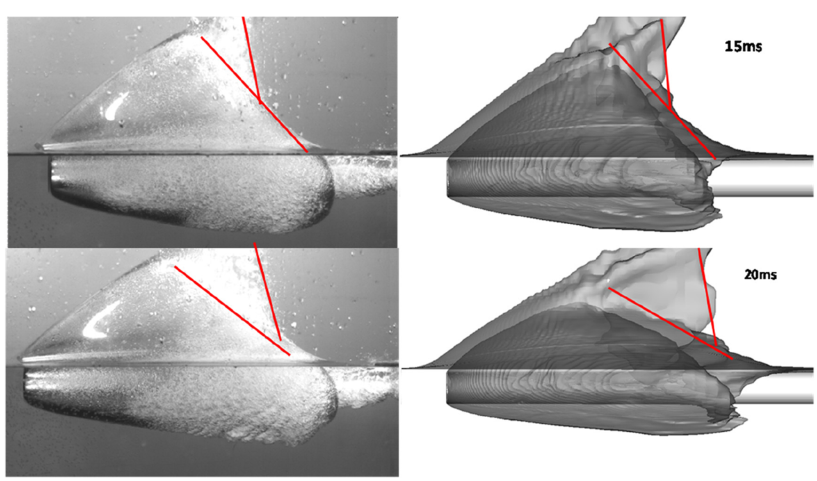

FIG. 12. Cavity development in the water layer falling process. The left and right views are the experiment photograph and the iso-surface of 90% water volume fraction at each moment, respectively. The red lines present the boundaries of the broken water layer.

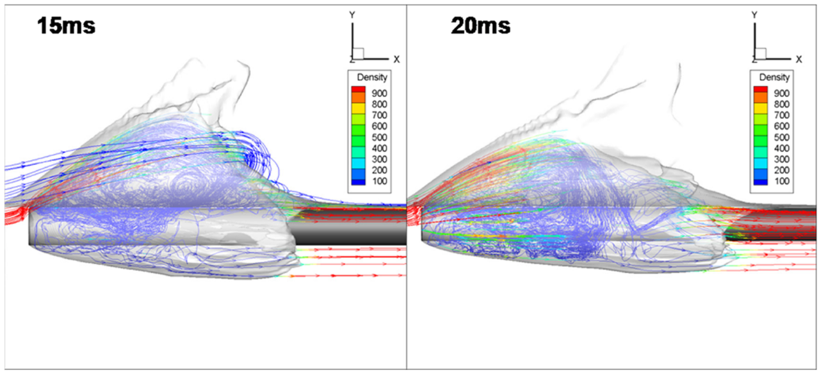

FIG. 13. Streamlines inside and around the cavity when the water layer falls and the access closes. The color of streamlines presents the density of the mixture, in which red means that the liquid phase is dominant, whereas blue means that the gas phase (vapor or air) is dominant.

B. Discussion of various headforms of the projectile

This subsection discusses two more types of headforms of the projectile: conical head and hemisphere head. Together with the preceding blunt head projectile mentioned, the experimental results and observations of the three cases are compared. Cavity evolution is compared in Figure 14, which shows that the blunt head projectile experienced the strongest air entertainment into the cavitating flow around the model, while the hemisphere head projectile experienced the weakest. Supercavity only occurs on the first two types of headforms. Natural ventilation occurs on the hemisphere head projectile with strong air entertainment into the cavity on the model.[43] A sharp shoulder of the projectile could induce a strong super cavity on the tested model.

Figure 15 plots the comparison of the variation of cavity lengths to clearly show the differences. The cavity length continues to grow during the water tank experiment for the supercavity on the blunt head projectile. However, for the two other cases, the length of the cavitating flow around the model is stable after the growth period. Wang analyzed the free surface effect on the cavitating flow around the underwater launched vehicle, which could induce a stable cavity on the tested model.[42]

C. Discussion of various cavitation numbers

This subsection discusses the results of the launching speed approximately 14, 16, 18, 20, and 24 m/s for the tested blunt head projectile in the water tank experiment, which are related to the

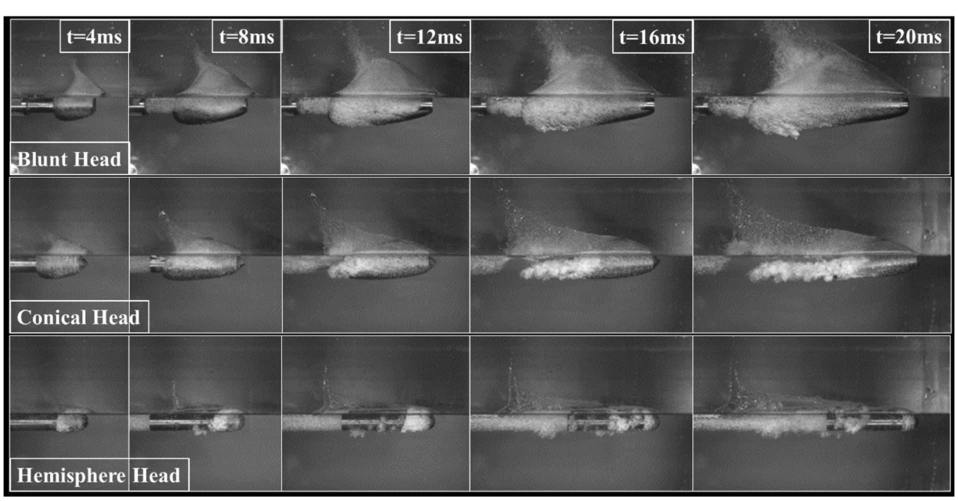

FIG. 14. Comparison of the blunt, conical, and hemisphere head projectile cavity evolution at 4, 8, 12, 16, and 20 ms.

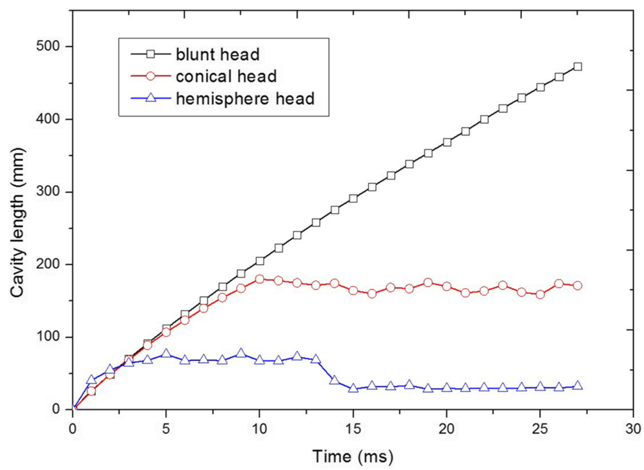

FIG. 15. Comparison of the variation of cavity lengths. The results of the three types of headforms of the projectile contain the blunt, conical, and hemisphere heads.

cavitation number of 1, 0.77, 0.61, 0.49, and 0.34, respectively, based on Equation (1) in Section II. Figure 16 plots the comparison of the variation of cavity lengths for different cavitation numbers. The super cavity on the projectile becomes strong as the model speed increases. The growth rate is proportional to the model speed. The growth rate of the cavity length is approximately similar to the model speed.

D. Vortex structures inside the bubble

The strong interactions in the cavity growth process occur between air entrainment and flow field inside the cavity, and large amounts of vortices are generated. An important concentrated vortex zone exists near the access inside the cavity, which presents strong interactions between air entrainment and the leaping water layer interface. A vortex with red surface is generated at 2 and 4 ms, which demonstrates that air entrainment tangentially moves along the outer cavity boundary when the cavity is short, as shown in Figures 17(a) and 17(b). The vortices nearly break down and are located near the projectile wall at 6 and 8 ms, which demonstrates a strong interaction between air entrainment and the boundary layer, as shown in Figures 17(c) and 17(d). The vortex structures nearly have blue and red colors above and below the middle horizontal plane, respectively. The color distribution can verify the preceding air entrainment trajectory mentioned.

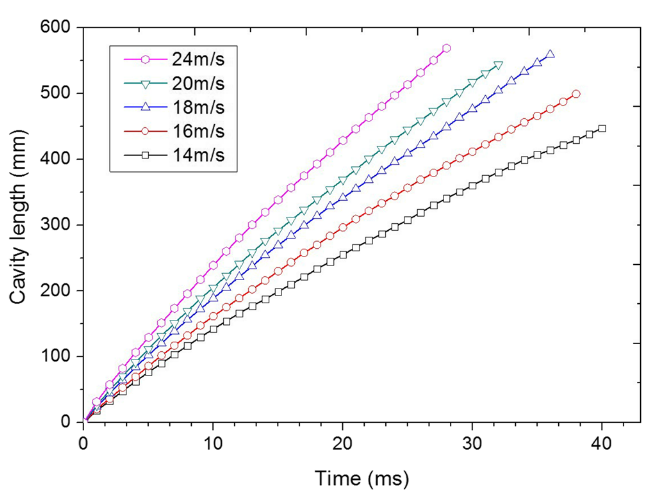

FIG. 16. Comparison of the variation of cavity lengths. The results of the tested speed of 14, 16, 18, 20, and 24 m/s are plotted.

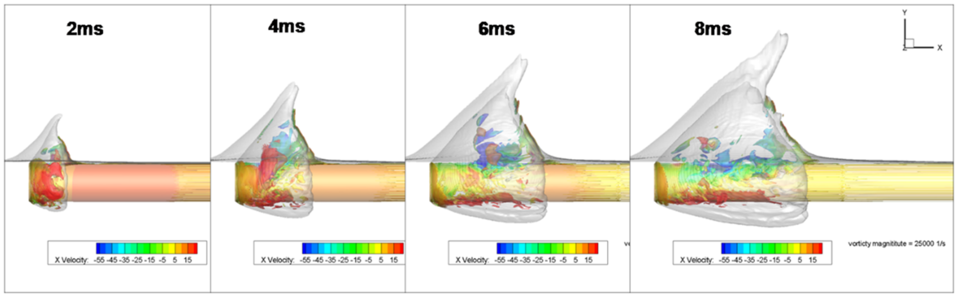

FIG. 17. Time sequence of cavity boundaries and vortex structures (1). The translucent surfaces are the cavity boundaries presented by the iso-surfaces of the water volume fraction of 90%. The vortex structures are presented by the iso-surfaces of the vorticity magnitude of 25000 1/s. The color presents the velocity in the axial direction, in which red means that velocity is the same as the main in flow, and blue means the opposite.

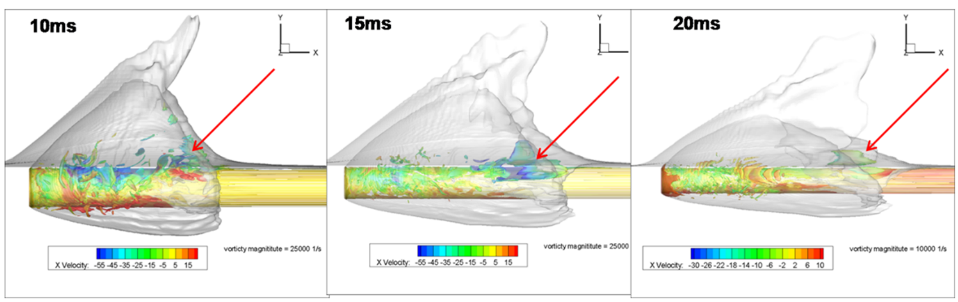

FIG. 18. Time sequence of cavity boundaries and vortex structures (2). The translucent surfaces are the cavity boundaries presented by the iso-surfaces of the water volume fraction of 90%. The vortex structures are presented by the iso-surfaces of the vorticity magnitude of 25000 1/s. The color presents the velocity in the axial direction, in which red means the velocity is the same as the main in flow, and blue means the opposite.

The vortex structure pattern at 10 ms is similar to that at 8 ms, as shown in Figure 18(a). Air entrainment velocity and vortex intensity both decrease as the water layer falls, as shown in Figure 18(b). When the water layer comes in contact with the projectile wall again, air entrainment inside the cavity weakens and loses its original trajectory, as shown in Figure 18(c).

E. Effect of supercavity on drag reduction

The good frictional drag reduction of artificial supercavity is the main reason for its application. Therefore, investigating whether the proposed new phenomenon can lead to a drag reduction effect is necessary. An additional submerged case is introduced with the same projectile model, launch speed, and numerical methods, while only the submerged depth is modified far from the projectile. Drag comparison is performed between the two cases. The projectile surface is divided into several subzones (Figure 19) to reflect the effects on various drag components, such as pressure and viscous drags.

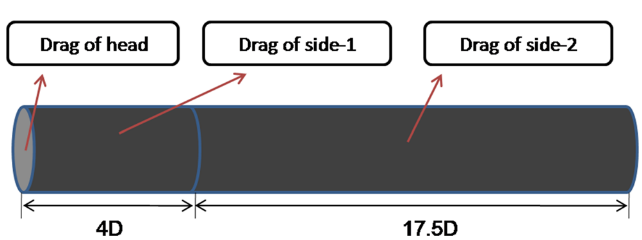

FIG. 19. Subzone division of the projectile surface.

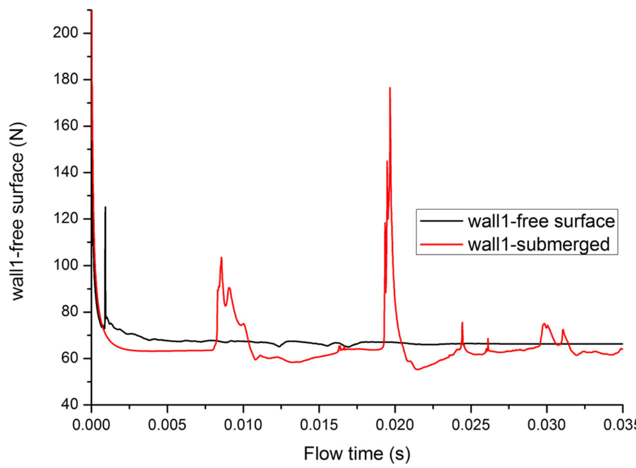

FIG. 20. Comparison of drags of head subzones. Black and red lines present the time variations of the drag in the free surface case and submerged case, respectively.

Drag time variation is obtained for each subzone. The head subzone drag in the supercavity case is more stable and higher than that in the submerged case due to the additional wave elevation effect. However, the drag in the submerged case is unstable and has local peak values due to local high pressure generated by cavity shedding and collapse, as shown in Figure 20.

The drag of the side wall is generated by a viscous effect. For the upstream part of the side wall, the drag in the free surface is also stable due to the intact supercavity. Meanwhile, the drag often varies in the submerged case due to cavity shedding and re-entry jet, as shown in Figure 21. Therefore, drag reduction is notable for this subzone in the free surface.

The drags for the long downstream parts of the side wall are stable. The drag of this subzone in the free surface case is significantly lower than that of the fully wet subzone in the submerged case due to the surrounding supercavity. The amplitude of drag reduction is nearly 50% for the stable values, as shown in Figure 22.

The total drags of the preceding subzones mentioned are compared, as shown in Figure 23. The drag in the free surface case stably decreased with time. Drag oscillations occur in the submerged case due to unsteady characteristics.

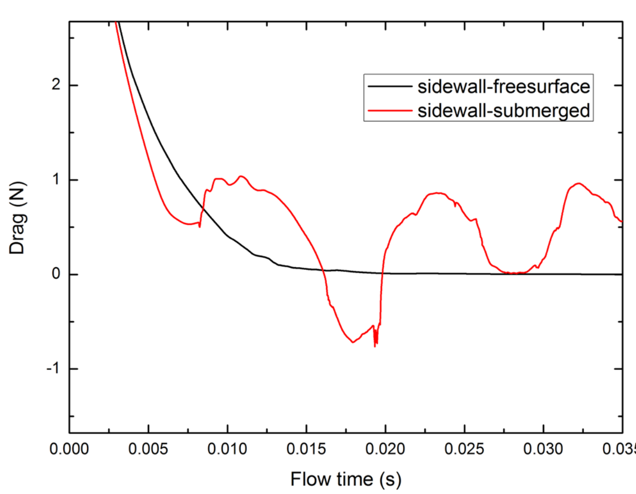

FIG. 21. Comparison of drags of upstream side subzones. Black and red lines present the time variations of the drag in the free surface case and submerged case, respectively.

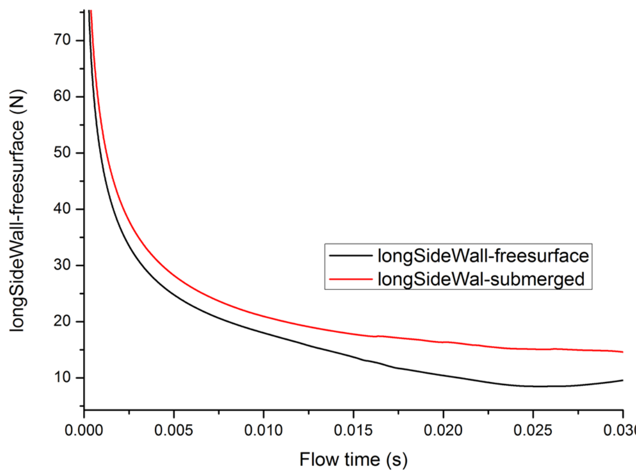

FIG. 22. Comparison of drags of the downstream side subzones. Black and red lines present the time variations of drag in the free surface and submerged cases, respectively.

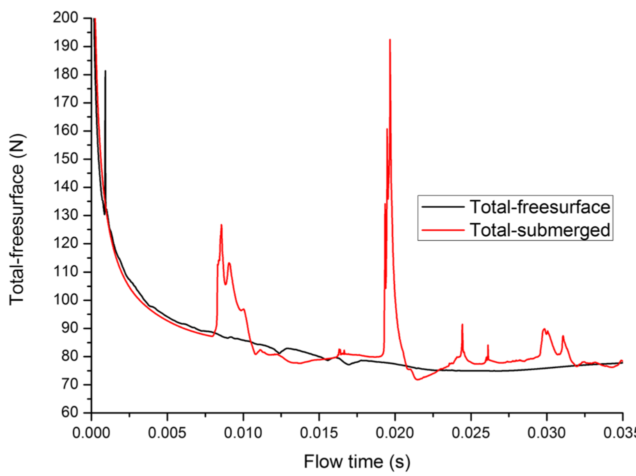

FIG. 23. Comparison of total drags. Black and red lines present the time variations of drag in the free surface and submerged cases, respectively.

Table I lists the time average values of the drags from 5 ms to 35 ms. Compared with the submerged case, the pressure drag of the head subzone is slightly higher, and viscous drags of the two other subzones are significantly lower in the free surface case. The relative difference of the total drag is approximately 4%. Therefore, viscous drag reduction by the supercavity near the free surface is more significant than the increase of pressure drag by wave elevation, which indicates that the present strategy near the free surface is effective for high-speed cruising.

TABLE I. Drag comparison of various subzones.

Subzones (Near free surface)	Drag(N)	Subzones (submerged)	Drag(N)
Head	66.6	Head	65.3
Side-leading(4D)	0.2	Side-leading(4D)	0.5
Side-trailing(17.5D)	12.9	Side-trailing(17.5D)	17.5
Total	79.7	Total	83.3

V. CONCLUSIONS

This study presents an experiment on the supercavitating flow around the axisymmetric projectile near the free surface. A numerical simulation is performed based on VOF and LES methods. The unsteady behaviors of the cavity and the water layer are obtained, and agreements are achieved between numerical and experimental results.

The supercavity is generated by the entrainment of a considerable amount of air into the cavity, which can cause the pressure increase inside and outside the cavity. Therefore, the actual cavitation number is close to zero, and a stable supercavity can be formed in the short-term cruising process. The air entrainment access is surrounded by the leaping water layer. The water layer breaks down and falls to the projectile surface, which can block air entrainment and lead to a shorter cavity on the upper side than that on the lower part of the projectile. Effect of various headforms of the projectile and cavitation numbers on the cavitating flow are also analyzed.

Air entrainment is fast and has a certain trajectory, which can form complex vortex structures by interacting with the flow field inside the cavity, which is also weakened by the falling of the broken water layer after the cavity growth process. Compared with the submerged case, the pressure drag of the head subzone is slightly higher, while the viscous drags of the two other subzones are significantly lower on the free surface. The relative difference of the total drag is approximately 4%.

The supercavity generated when the projectile is close and piercing the free surface is stable, by which the cavitation erosion effect due to unstable cavitation can be neglected. In addition, drag reduction effect in the present case is more significant than the submerged case. The results of this study reveal that the present strategy near the free surface can be a new effective approach for high-speed cruising after vigorous design optimization in the future.

ACKNOWLEDGMENTS

The authors are grateful to the national natural science foundation of China through grant numbers 11772340 & 11672315. This project was also supported by the Youth Innovation Promotion Association CAS (2015015).

[1] C. E. Brennen, *Cavitation and bubble dynamics* (Oxford University Press, USA, 1995).
[2] R. T. Knapp, J. W. Daily, and F. G. Hammitt, *Cavitation* (McGraw-Hill, 1970).
[3] M. R. Pendar and E. Roohi, "Investigation of cavitation around 3D hemispherical head-form body and conical cavitators using different turbulence and cavitation models," Ocean Engineering **112**, 287–306 (2016).
[4] E. Roohi, M. R. Pendar, and A. Rahimi, "Simulation of three-dimensional cavitation behind a disk using various turbulence and mass transfer models," Applied Mathematical Modelling **10**, 12–13 (2015), 32, 42–13 passim.
[5] M. Dular, R. Bachert, B. Stoffel, and B. Sirok, "Experimental evaluation of numerical simulation of cavitating flow around hydrofoil," European Journal of Mechanics - B/Fluids **24**, 522–538 (2005).
[6] B. Stutz and J. L. Reboud, "Experiments on unsteady cavitation," Experiments in Fluids **22**, 191–198 (1997).
[7] B. Stutz and J. L. Reboud, "Measurements within unsteady cavitation," Experiments in Fluids **29**, 545–552 (2000).
[8] V. Aeschlimann, S. Barre, and S. Legoupil, "X-ray attenuation measurements in a cavitating mixing layer for instantaneous two-dimensional void ratio determination," Physics of Fluids **23**, 253–268 (2011).
[9] I. Khlifa and O. Coutier-Delgosha, "Velocity measurements in cavitating flows using fast x-ray imaging," in Congrés Français de Mécanique, France, 2013.
[10] S. A. Mäkiharju, C. Gabillet, B. G. Paik, N. A. Chang, M. Perlin, and S. L. Ceccio, "Time-resolved two-dimensional x-ray densitometry of a two-phase flow downstream of a ventilated cavity," Experiments in Fluids **54**, 1–21 (2013).
[11] R. F. Kunz, D. A. Boger, D. R. Stinebring, T. S. Chyczewski, J. W. Lindau, H. J. Gibeling, S. Venkateswaran, and T. R. Govindan, "A preconditioned Navier-Stokes method for two-phase flows with application to cavitation prediction," Computers & Fluids **29**, 849–875 (2000).
[12] C. L. Merkle, J. Feng, and P. E. O. Buelow, "Computational modeling of the dynamics of sheet cavitation," in Proc 3rd International Symposium on Cavitation, Grenoble, France, 2001.
[13] A. K. Singhal, M. M. Athavale, H. Li, and Y. Jiang, "Mathematical basis and validation of the full cavitation model," Journal of Fluids Engineering **124**, 617–624 (2002).
[14] X. Long, H. Cheng, B. Ji, R. E. A. Arndt, and X. Peng, "Large eddy simulation and Euler-Lagrangian coupling investigation of the transient cavitating turbulent flow around a twisted hydrofoil," International Journal of Multiphase Flow (2017).
[15] Q. Wu, B. Huang, G. Wang, and S. Cao, "The transient characteristics of cloud cavitating flow over a flexible hydrofoil," International Journal of Multiphase Flow (2017).
[16] O. Coutier-Delgosha, F. Deniset, J. A. Astolfi, and J. Leroux, "Numerical prediction of cavitating flow on a two-dimensional symmetrical hydrofoil and comparison to experiments," Journal of Fluids Engineering **129**, 279 (2007).
[17] O. Coutier-Delgosha, R. Fortes-Patella, and J. L. Reboud, "Evaluation of the turbulence model influence on the numerical simulations of unsteady cavitation," Journal of Fluids Engineering **125**, 38 (2003).

[18] O. Coutier-Delgosha, B. Stutz, A. Vabre, and S. Legoupil, "Analysis of cavitating flow structure by experimental and numerical investigations," Journal of Fluid Mechanics **578**, 171–222 (2007).
[19] L. Zhou and Z. Wang, "Numerical simulation of cavitation around a hydrofoil and evaluation of a RNG κ-ε model," Journal of Fluids Engineering **130**, 011302 (2008).
[20] O. Coutier-Delgosha, J. L. Reboud, and Y. Delannoy, "Numerical simulation of the unsteady behaviour of cavitating flows," International Journal for Numerical Methods in Fluids **42**, 527–548 (2003).
[21] J. Y. Wu, G. Y. Wang, and W. Shyy, "Time-dependent turbulent cavitating flow computations with interfacial transport and filter-based models," International Journal for Numerical Methods in Fluids **49**, 739–761 (2005).
[22] B. Huang, Y. Zhao, and G. Wang, "Large eddy simulation of turbulent vortex-cavitation interactions in transient sheet/cloud cavitating flows," Computers & Fluids **92**, 113–124 (2014).
[23] B. Ji, X. Luo, R. E. A. Arndt, and Y. Wu, "Numerical simulation of three dimensional cavitation shedding dynamics with special emphasis on cavitation-vortex interaction," Ocean Engineering **87**, 64–77 (2014).
[24] B. Huang, G.-y. Wang, and Y. Zhao, "Numerical simulation unsteady cloud cavitating flow with a filter-based density correction model," Journal of Hydrodynamics **26**, 26–36 (2014).
[25] R. E. Bensow and G. Bark, "Implicit LES predictions of the cavitating flow on a propeller," Journal of Fluids Engineering-Transactions of the ASME **132**, 041302 (2010).
[26] L. Li, Q. Jia, Z. Liu, B. Li, Z. Hu, and Y. Lin, "Eulerian two-phase modeling of cavitation for high-speed UUV using different turbulence models," in Cyber Technology in Automation, Control, and Intelligent Systems (CYBER), 2015 IEEE International Conference on, IEEE, 2015, pp. 1247–1252.
[27] N. Dittakavi, A. Chunekar, and S. Frankel, "Large eddy simulation of turbulent-cavitation interactions in a venturi nozzle," Journal of Fluids Engineering-Transactions of the ASME **132** (2010).
[28] E. Roohi, A. P. Zahiri, and M. Passandideh-Fard, "Numerical simulation of cavitation around a two-dimensional hydrofoil using VOF method and LES turbulence model," Applied Mathematical Modelling **37**, 6469–6488 (2013).
[29] X. Yu, C. Huang, T. Du, L. Liao, X. Wu, Z. Zheng, and Y. Wang, "Study of characteristics of cloud cavity around axisymmetric projectile by large eddy simulation," Journal of Fluids Engineering-Transactions of the ASME **136** (2014).
[30] A. Gnanaskandan and K. Mahesh, "A numerical method to simulate turbulent cavitating flows," International Journal of Multiphase Flow **70**, 22–34 (2015).
[31] S. L. Ceccio, "Friction drag reduction of external flows with bubble and gas injection," Annual Review of Fluid Mechanics **42**, 183–203 (2010).
[32] C. L. Merkle and S. Deutsch, "Microbubble drag reduction in liquid turbulent boundary layers," Applied Mechanics Reviews **45**, 103–127 (1992).
[33] X. Shen, S. L. Ceccio, and M. Perlin, "Influence of bubble size on micro-bubble drag reduction," Experiments in Fluids **41**, 415–424 (2006).
[34] B. R. Elbing, S. Mäkiharju, A. Wiggins, M. Perlin, D. R. Dowling, and S. L. Ceccio, "On the scaling of air layer drag reduction," Journal of Fluid Mechanics **717**, 484–513 (2013).
[35] B. R. Elbing, E. S. Winkel, K. A. Lay, S. L. Ceccio, D. R. Dowling, and M. Perlin, "Bubble-induced skin-friction drag reduction and the abrupt transition to air-layer drag reduction," Journal of Fluid Mechanics **612**, 201–236 (2008).
[36] X. Yu, Y. Wang, C. Huang, Y. Wei, X. Fang, T. Du, and X. Wu, "Experiment and simulation on air layer drag reduction of high-speed underwater axisymmetric projectile," European Journal of Mechanics - B/Fluids **52**, 45–54 (2015).
[37] E. Kawakami and R. E. Arndt, "Investigation of the behavior of ventilated supercavities," Journal of Fluids Engineering **133**, 091305 (2011).
[38] W. Zou, K. P. Yu, R. E. A. Arndt, G. Zhang, and Z. W. Li, "On the shedding of the ventilated supercavity with velocity disturbance," Ocean Engineering **57**, 223–229 (2013).
[39] Z. Wang, B. Huang, G. Wang, M. Zhang, and F. Wang, "Experimental and numerical investigation of ventilated cavitating flow with special emphasis on gas leakage behavior and re-entrant jet dynamics," Ocean Engineering **108**, 191–201 (2015).
[40] T. T. Truscott, B. P. Epps, and J. Belden, "Water entry of projectiles," Annual Review of Fluid Mechanics **46**, 355–378 (2014).
[41] M. Lee, R. Longoria, and D. Wilson, "Cavity dynamics in high-speed water entry," Physics of Fluids (1994-present) **9**, 540–550 (1997).
[42] Y. Wang, X. Wu, C. Huang, and X. Wu, "Unsteady characteristics of cloud cavitating flow near the free surface around an axisymmetric projectile," International Journal of Multiphase Flow **85**, 48–56 (2016).
[43] Y. Wang, X. Wu, and C. Huang, "Ventilated partial cavitating flow around a blunt body near the free surface," in ISROMAC 2016: International Symposium on Transport Phenomena and Dynamics of Rotating Machinery, 2016, pp. 6.
[44] S. Bal, "A numerical method for the prediction of wave pattern of surface piercing cavitating hydrofoils," Proceedings of the Institution of Mechanical Engineers, Part C: Journal of Mechanical Engineering Science **221**, 1623–1633 (2007).
[45] S. Bal, "Prediction of wave pattern and wave resistance of surface piercing bodies by a boundary element method," International Journal for Numerical Methods in Fluids **56**, 305–329 (2008).
[46] Y. Young and S. Kinnas, "Analysis of supercavitating and surface-piercing propeller flows via BEM," Computational Mechanics **32**, 269–280 (2003).
[47] O. Faltinsen, "Hydrodynamics of high speed marine vehicles," in Hydrodynamics VI: Theory and Applications: Proceedings of the 6th International Conference on Hydrodynamics, Perth, Western Australia, 24-26 November 2004, CRC Press, 2004, pp. 3.
[48] EchoBeluga(2014.1.17), Katina's Fast Swim [Video file], in, 2014.
[49] O. M. Faltinsen and Y. A. Semenov, "The effect of gravity and cavitation on a hydrofoil near the free surface," Journal of Fluid Mechanics **597**, 371–394 (2008).
[50] Y. P. Wei, Y. W. Wang, X. Fang, C. G. Huang, and Z. P. Duan, "A scaled underwater launch system accomplished by stress wave propagation technique," Chinese Physics Letters **28**, 024601–024672 (2011).

[51] P. J. Zwart, G. A. Gerber, and T. Belarmri, "A two-phase on model for predicting cavitation dynamics," in Fifth International Conference on Multi-phase Flow, Yokohama, Japan, 2004.
[52] X. Yu, Y. Wang, C. Huang, and T. Du, "Study on the influence of phase change rate on cloud cavitation," Procedia Engineering **61**, 204–206 (2013).
[53] P. J. Zwart, G. A. Gerber, and T. Belarmri, "A two-phase on model for predicting cavitation dynamics," in Fifth International Conference on Multi-phase Flow, Yokohama, Japan, 2004.